Sound & Vibration 2026, 60(6), 4699.
doi: https://doi.org/10.59400/sv4699

Article

Interval type-2 fuzzy α-plane minimax co-design of multi-tuned mass dampers for broadband vibration control under bounded uncertainty

Suleiman Ibrahim Mohammad[1], Yogeesh Nijalingappa[1,2,3,*], Seif Al Bustanji[4,5], Poornachandran William[6,7], Asokan Vasudevan[8]

[1] Research Fellow, INTI International University, Nilai 71800, Malaysia; dr_sliman@yahoo.com
[2] Mathematics & Natural Sciences, Gulf University for Science & Technology, Safat 13060, Kuwait
[3] Department of Mathematics, Government First Grade College, Tumkur 572102, India
[4] Faculty of Technical Education, Al-Ahliyya Amman University, Amman 19328, Jordan; s.albustanji@ammanu.edu.jo
[5] Hourani Center for Applied Scientific Research (HCASR), Al-Ahliyya Amman University, Amman 19328, Jordan
[6] School of Computer Science and Technology, Karunya Institute of Technology and Sciences, Coimbatore 641114, India; williamp@karunya.edu
[7] Research and Consultancy Centre, UNITAR International University, Petaling Jaya 47301, Malaysia
[8] Faculty of Business and Communications, INTI International University, Nilai 71800, Malaysia; asokan.vasudevan@newinti.edu.my
*** Corresponding author:** Yogeesh Nijalingappa, yogeesh.n@ka.gov.in

CITATION

Mohammad SI, Nijalingappa Y, Al Bustanji S, et al. Interval type-2 fuzzy α-plane minimax co-design of multi-tuned mass dampers for broadband vibration control under bounded uncertainty. Sound & Vibration. 2026; 60(6): 4699. https://doi.org/10.59400/sv4699

ARTICLE INFO

Received: 20 July 2026
Revised: 1 August 2026
Accepted: 14 August 2026
Available online: 24 August 2026

Abstract: Passive tuned mass dampers are effective near their design frequencies but can lose performance or exceed travel limits when structural properties are imprecise. This paper develops an interval type-2 fuzzy α-plane minimax method for the simultaneous allocation, tuning, and damping design of a three-absorber bank on a six-degree-of-freedom coupled machine–foundation system. Primary mass, stiffness, and damping are represented by lower and upper triangular membership functions, so uncertainty in both parameter values and membership widths is retained. At every α-plane, outer and inner vertex responses are propagated through the complex frequency-response matrix. A membership-weighted objective combines worst peak acceleration, broadband root-mean-square acceleration, footprint width, and a 16 mm relative-stroke constraint. Differential evolution determines nine absorber variables for a fixed 6% auxiliary-mass budget. The frequency-domain solver reproduces classical equal-peak tuning ratios to machine precision and absorber damping ratios within 0.20%. In 2,048 independent outer-support Sobol scenarios, the proposed design decreases the mean peak acceleration from 6.058 g to 1.262 g and the worst peak acceleration from 9.005 g to 1.682 g. The deterministic optimum attains a smaller mean peak of 1.112 g but violates the stroke constraint in 55.42% of the scenarios; the type-1 robust design violates it in 2.05%, whereas the proposed design has no violations and a maximum stroke of 15.992 mm. The results show that explicitly preserving membership-function uncertainty changes the mass allocation and first-mode detuning sufficiently to obtain a feasible broadband design without active control.

Keywords: epistemic imprecision; machinery–foundation dynamics; frequency-response envelope; absorber travel; differential evolution; out-of-sample stress testing

1. Introduction

Harmonic excitation traverses several modes in rotating machinery and frames, degrading accuracy and structural life. A tuned mass damper splits resonance through an auxiliary mass–spring–damper [1–5], but performance depends on tuning, damping, location, travel, modal coupling, and uncertain properties.

Slowest optimizations have been the single-mode benchmark: Warburton considered multiple excitation-response cases [6], Krenk specified the frequency-domain solution [7], and Nishihara, Asami and co-workers extracted minimax and energy-optimal formulae for damped hosts [8,9]. Stiffness shifts detune antiresonance and modal coupling transfer amplification, when based on frequency and mass ratios.

MTMDs are distributed by minimal design or multi-degree-of-freedom, such as through mass–stiffness minimax design [10], stiffness–damping optimization [11], ensemble characterization [12], modal optimization [13] and bi-tuned formulas [14]. Optimizing equal masses and modal tuning (damping, multiple outputs or constraints on the stroke could change), but excessive travel would make a design impractical.

Uncertainty weakens nominal designs. Robust formulations account for variance, reliability, bounds on the variables, stochastic loading, and worst-case scenarios [15], generally resulting in solutions that are distinct from deterministic optima [16]. The fuzzy criteria bypass presumed probability rules [17, 18] and methods of reliability [19–21], serviceability design [22], as well as incorporating a hybrid aleatory–epistemic model approach [23]. Probability models can imply unjustified precision when repeated data or defensible joint distributions are unavailable. Recent interval-based structural optimization, including interval Taylor expansion, provides a complementary way to propagate bounded epistemic uncertainty [24,25].

Interval type-2 fuzzy sets retain upper and lower membership functions when both a parameter and the grade assigned to its admissible values are uncertain [26,27]; constrained forms further restrict the admissible embedded sets [28]. Probability-based models require defensible distributions, whereas a type-1 fuzzy model treats one membership function as exact. The interval type-2 representation is therefore used here to preserve second-order epistemic uncertainty in the membership widths of stiffness, mass, and damping rather than collapsing all expert or tolerance information into a single triangular membership function.

Robust optimization seeks satisfactory performance under uncertainty [29, 30]. Differential evolution can handle nonconvex responses without gradients [31]; NSGA-II supports peak–energy trade-off studies [32]; and sensitivity analysis diagnoses influential variables [33]. Recent developments include MTMD placement and parameter optimization [2, 34, 35], double absorbers, TMD–inerter systems [36], and surrogate-assisted robust TMD design [17, 20]. Membership uncertainty, multimodal peak/RMS suppression, and a hard stroke limit remain uncombined.

This study models bounded epistemic uncertainty with interval type-2 fuzzy sets, not active control. Inner and outer α-cut vertices enter the complex dynamic-stiffness matrix, and three absorbers are co-designed under a 6% mass budget and 16 mm travel limit. Closed-form verification precedes 2,048-scenario independent Sobol validation on a reproducible six-degree-of-freedom benchmark spanning 5.15–35.13 Hz.

2. Materials and methods

2.1. Coupled primary system

The primary structure is a six-degree-of-freedom chain representing the dominant lateral coordinates of a compact machine–foundation assembly. The model is deliberately stated in physical units and is used as a numerical benchmark; no experimental identification is claimed. Let $\mathrm{x}(t) \in \mathbb{R}^6$ denote the displacement vector. Under a multi-point harmonic force, the nominal equations are:

$$\mathrm{M}_0\ddot{\mathrm{x}}(t) + \mathrm{C}_0\dot{\mathrm{x}}(t) + \mathrm{K}_0\mathrm{x}(t) = \Re\left\{\mathrm{F}\, e^{\mathrm{i}\omega t}\right\} \tag{1}$$

The diagonal mass matrix is:

$$\mathrm{M}_0 = \mathrm{diag}(92, 76, 68, 61, 54, 47)\ \mathrm{kg} \tag{2}$$

and the six coupling stiffnesses, beginning with the ground-to-first-coordinate spring, are:

$$\mathrm{k} = 10^6(1.30, 1.10, 0.96, 0.82, 0.70, 0.60)^{\mathsf{T}}\ \mathrm{N\,m^{-1}} \tag{3}$$

For $n = 6$, assembly gives the symmetric tridiagonal matrix:

$$K_{ij} = \begin{cases} k_1 + k_2, & i = j = 1, \\ k_i + k_{i+1}, & 1 < i = j < n, \\ k_n, & i = j = n, \\ -k_{i+1}, & j = i+1 \text{ or } i = j+1, \\ 0, & \text{otherwise.} \end{cases} \tag{4}$$

The undamped generalized eigenproblem is:

$$\left(\mathrm{K}_0 - \omega_r^2\mathrm{M}_0\right)\phi_r = 0, \qquad \phi_r^{\mathsf{T}}\mathrm{M}_0\phi_s = \delta_{rs} \tag{5}$$

It yields natural frequencies $f_r = \omega_r/(2\pi)$ of 5.1517, 13.0614, 20.5066, 26.8221, 31.6825, and 35.1271 Hz. Rayleigh damping is used so that the first and third modal damping ratios are 0.015 and 0.025:

$$\mathrm{C}_0 = a_R\mathrm{M}_0 + b_R\mathrm{K}_0 \tag{6}$$

$$\begin{bmatrix} (2\omega_1)^{-1} & \omega_1/2 \\ (2\omega_3)^{-1} & \omega_3/2 \end{bmatrix}\begin{bmatrix} a_R \\ b_R \end{bmatrix} = \begin{bmatrix} 0.015 \\ 0.025 \end{bmatrix} \tag{7}$$

The resulting coefficients are $a_R = 0.60251\ \mathrm{s}^{-1}$ and $b_R = 3.5177 \times 10^{-4}$ s. Two coherent forces are applied: $F_1 = 420$ N at coordinate 1 and $F_3 = 220e^{\mathrm{i}\pi/6}$ N at coordinate 3. Coordinates 2, 4, and 6 are monitored (see **Table 1**). The excitation interval is 3.5–23.5 Hz, which contains the first three primary resonances and represents a run-up band rather than a single operating speed.

Table 1. Primary-system parameters and modal properties.

Coordinate	Mass (kg)	Coupling stiffness (MN m^{-1})	Natural frequency (Hz)	Nominal modal damping (%)	Monitored
1	92	1.30	5.1517	1.500	No
2	76	1.10	13.0614	1.811	Yes
3	68	0.96	20.5066	2.500	No
4	61	0.82	26.8221	3.143	Yes
5	54	0.70	31.6825	3.653	No
6	47	0.60	35.1271	4.018	Yes

Figure 1 shows the assembled benchmark and the attachment arrangement. Absorbers 1 and 2 are placed at coordinate 6, where the first two mass-normalized modes have large amplitudes, and absorber 3 is placed at coordinate 4, which has a large third-mode amplitude. Attachment locations are fixed so that the optimization focuses on physically continuous variables.

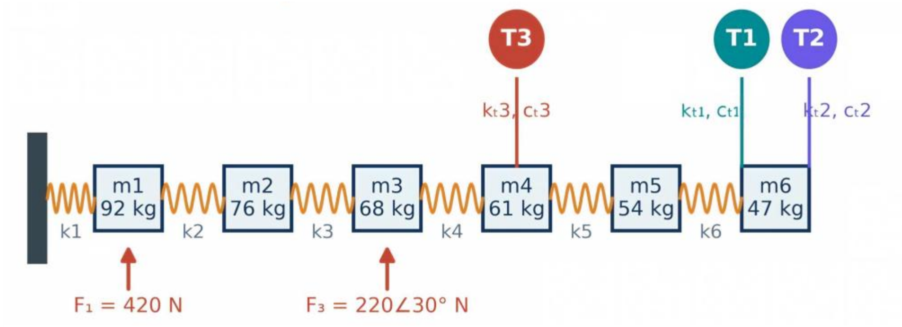

Figure 1. Six-degree-of-freedom coupled machine–foundation benchmark, harmonic forces, and three-absorber bank.

2.2. Augmented multi-absorber dynamics

Let absorber $j \in \{1,2,3\}$ have mass m_{tj}, stiffness k_{tj}, damping c_{tj}, and attachment coordinate $p_j \in \{6,6,4\}$. Its uncoupled natural frequency and damping ratio are:

$$\omega_{tj} = \sqrt{\frac{k_{tj}}{m_{tj}}}, \qquad \zeta_{tj} = \frac{c_{tj}}{2m_{tj}\omega_{tj}} \tag{8}$$

With $\mathrm{q} = \left[\mathrm{x}^{\mathsf{T}}, y_1, y_2, y_3\right]^{\mathsf{T}}$, the controlled system has nine coordinates:

$$\mathrm{M}_a\ddot{\mathrm{q}} + \mathrm{C}_a\dot{\mathrm{q}} + \mathrm{K}_a\mathrm{q} = \Re\left\{\mathrm{F}_a e^{\mathrm{i}\omega t}\right\} \tag{9}$$

For the unit vector $\mathrm{e}_{p_j} \in \mathbb{R}^6$ and absorber selector $\mathrm{e}_{6+j} \in \mathbb{R}^9$, define the relative-motion vector:

$$\mathrm{b}_j = \begin{bmatrix} \mathrm{e}_{p_j} \\ -\mathrm{e}_j \end{bmatrix} \in \mathbb{R}^9 \tag{10}$$

The augmented matrices are compactly written as:

$$\mathrm{M}_a = \begin{bmatrix} \mathrm{M} & 0 \\ 0 & \operatorname{diag}(m_{t1}, m_{t2}, m_{t3}) \end{bmatrix} \tag{11}$$

$$\mathrm{K}_a = \begin{bmatrix} \mathrm{K} & 0 \\ 0 & 0 \end{bmatrix} + \sum_{j=1}^{3} k_{tj}\mathrm{b}_j\mathrm{b}_j^{\mathsf{T}} \tag{12}$$

$$\mathrm{C}_a = \begin{bmatrix} \mathrm{C} & 0 \\ 0 & 0 \end{bmatrix} + \sum_{j=1}^{3} c_{tj}\mathrm{b}_j\mathrm{b}_j^{\mathsf{T}} \tag{13}$$

The total primary mass is 398 kg. A fixed auxiliary-mass ratio $\mu_T = 0.06$ gives:

$$\sum_{j=1}^{3} m_{tj} = \mu_T \sum_{i=1}^{6} m_i = 0.06(398) = 23.88\ \mathrm{kg} \tag{14}$$

Three positive allocation variables w_j are normalized, preventing an equality-constraint violation during evolutionary search:

$$m_{tj} = 23.88 \frac{w_j}{\sum_{\ell=1}^{3} w_\ell}, \qquad 0.35 \leq w_j \leq 1.65 \tag{15}$$

This normalization enforces the 23.88 kg total-mass equality exactly and keeps all device masses positive without introducing a Lagrange multiplier or a penalty coefficient. Its drawbacks are that proportional scaling of all allocation variables represents the same mass fractions, the normalization couples the variables nonlinearly, and bounds on the auxiliary variables do not translate directly into independent bounds on each physical mass fraction. These effects can introduce redundancy or search bias, but they do not alter total-mass feasibility.

The tuning ratios are referenced to the first three nominal modal frequencies,

$$r_j = \frac{\omega_{tj}}{\omega_j}, \qquad 0.84 \leq r_j \leq 1.16 \tag{16}$$

and $0.035 \leq \zeta_{tj} \leq 0.24$. Thus the nine-dimensional design vector is:

$$\mathrm{d} = (w_1, w_2, w_3, r_1, r_2, r_3, \zeta_{t1}, \zeta_{t2}, \zeta_{t3})^{\mathsf{T}} \tag{17}$$

For any candidate vector, physical coefficients follow directly:

$$k_{tj} = m_{tj} \left(r_j \omega_j\right)^2, \qquad c_{tj} = 2\zeta_{tj} m_{tj} r_j \omega_j \tag{18}$$

2.3. Frequency-response measures and stroke constraint

At angular frequency ω, the complex dynamic stiffness and steady-state response are:

$$\mathrm{D}(\omega; \mathrm{d}, \theta) = \mathrm{K}_a - \omega^2 \mathrm{M}_a + \mathrm{i}\omega \mathrm{C}_a \tag{19}$$

$$\mathrm{Q}(\omega; \mathrm{d}, \theta) = \mathrm{D}^{-1}(\omega; \mathrm{d}, \theta) \mathrm{F}_a \tag{20}$$

Here, $\theta = (\theta_m, \theta_k, \theta_c)^{\mathsf{T}}$ contains uncertain multipliers applied to the primary matrices:

$$\mathrm{M} = \theta_m \mathrm{M}_0, \qquad \mathrm{K} = \theta_k \mathrm{K}_0, \qquad \mathrm{C} = \theta_c \mathrm{C}_0 \tag{21}$$

For monitored coordinate $s \in \mathcal{S} = \{2, 4, 6\}$, acceleration in gravitational units is

$$A_s(\omega) = \frac{\omega^2 \left|Q_s(\omega)\right|}{g_0}, \qquad g_0 = 9.80665 \ \mathrm{m\,s^{-2}} \tag{22}$$

The peak and broadband RMS measures on the grid $\Omega = 2\pi[3.5, 23.5]$ Hz are:

$$J_\infty(\mathrm{d}, \theta) = \max_{\omega \in \Omega} \max_{s \in \mathcal{S}} A_s(\omega) \tag{23}$$

$$J_2(\mathrm{d}, \theta) = \left[\frac{1}{3N_\omega} \sum_{\omega \in \Omega} \sum_{s \in \mathcal{S}} A_s^2(\omega)\right]^{1/2} \tag{24}$$

The relative travel of absorber j is:

$$S_j(\omega) = \left|Q_{6+j}(\omega) - Q_{p_j}(\omega)\right| \tag{25}$$

and the implementability condition is:

$$J_S(\mathrm{d}, \theta) = \max_{\omega\in\Omega} \max_{j} S_j(\omega) \leq S_{\max} = 0.016 \text{ m} \tag{26}$$

The peak measure protects the most severe resonance at any monitored coordinate, while the RMS measure prevents the optimizer from producing a narrow low peak at the cost of a generally elevated response over the rest of the run-up band. The stroke constraint is evaluated at every uncertainty vertex used by the robust objective.

2.4. Interval type-2 fuzzy uncertainty model

Each multiplier is centered at 1.0 and is assigned a lower triangular membership function (LMF) and a wider upper triangular membership function (UMF). For half-width $h > 0$,

$$\mu_\triangle(\theta; h) = \max\left(0, 1 - \frac{|\theta - 1|}{h}\right) \tag{27}$$

The interval type-2 membership grade is:

$$\mu_{\widetilde{\Theta}}(\theta) = \left[\underline{\mu}(\theta), \overline{\mu}(\theta)\right] = \left[\mu_\triangle\left(\theta; h_L\right), \mu_\triangle\left(\theta; h_U\right)\right], \qquad h_L \leq h_U \tag{28}$$

The footprint of uncertainty is therefore:

$$\mathrm{FOU}\left(\widetilde{\Theta}\right) = \bigcup_{\theta} \left\{(\theta, u) : \underline{\mu}(\theta) \leq u \leq \overline{\mu}(\theta)\right\} \tag{29}$$

At membership level $\alpha \in [0, 1]$, the inner and outer cuts are:

$$\Theta_\alpha^L = [1 - h_L(1-\alpha),\ 1 + h_L(1-\alpha)] \tag{30}$$

$$\Theta_\alpha^U = [1 - h_U(1-\alpha),\ 1 + h_U(1-\alpha)] \tag{31}$$

Mass, stiffness, and damping use $(h_L, h_U) = (0.03, 0.06)$, $(0.07, 0.12)$, and $(0.16, 0.30)$, respectively. The relatively wide damping footprint reflects the difficulty of assigning precise damping from limited operational information. **Figure 2** shows the three footprints, and **Table 2** lists representative cuts used in optimization.

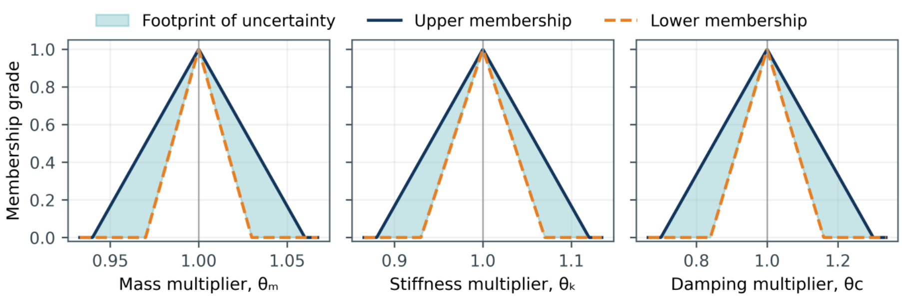

Figure 2. Lower and upper triangular membership functions for primary mass, stiffness, and damping multipliers.

Table 2. Inner and outer α-cut intervals for the interval type-2 fuzzy multipliers.

Multiplier	α	Inner cut	Outer cut
Mass, θ_m	0.0	[0.970, 1.030]	[0.940, 1.060]
	0.5	[0.985, 1.015]	[0.970, 1.030]
	1.0	[1.000, 1.000]	[1.000, 1.000]
Stiffness, θ_k	0.0	[0.930, 1.070]	[0.880, 1.120]
	0.5	[0.965, 1.035]	[0.940, 1.060]
	1.0	[1.000, 1.000]	[1.000, 1.000]
Damping, θ_c	0.0	[0.840, 1.160]	[0.700, 1.300]
	0.5	[0.920, 1.080]	[0.850, 1.150]
	1.0	[1.000, 1.000]	[1.000, 1.000]

For each $\alpha \in \{0, 0.5, 1\}$, the Cartesian product of the three cuts forms an inner box $\mathcal{B}_\alpha^L$ and an outer box $\mathcal{B}_\alpha^U$. The eight vertices of a nondegenerate box are propagated through Equations (19)–(25). The resulting α-level peak bounds are:

$$\overline{J}_{\infty,\alpha}^U(\mathrm{d}) = \max_{\theta \in \mathrm{vert}(\mathcal{B}_\alpha^U)} J_\infty(\mathrm{d}, \theta) \tag{32}$$

$$\overline{J}_{\infty,\alpha}^L(\mathrm{d}) = \max_{\theta \in \mathrm{vert}(\mathcal{B}_\alpha^L)} J_\infty(\mathrm{d}, \theta) \tag{33}$$

The difference

$$W_{\infty,\alpha}(\mathrm{d}) = \max\left(0, \overline{J}_{\infty,\alpha}^U - \overline{J}_{\infty,\alpha}^L\right) \tag{34}$$

quantifies performance ambiguity caused specifically by the uncertain membership width, not by the central mechanical model alone. Analogous outer maxima $\overline{J}_{2,\alpha}^U$ and $\overline{J}_{S,\alpha}^U$ are computed for RMS acceleration and stroke.

A conventional type-1 α-cut provides only one interval at each membership level and therefore treats its width as fixed. Here, the paired inner and outer α-cuts retain two admissible intervals at the same α-level; their response gap is propagated through the width terms in Equations (32)–(37). This inner–outer gap is the retained uncertainty in membership width, not an additional probability distribution.

2.5. Robust objective and comparison designs

Let the membership-level weights for $\alpha = (0, 0.5, 1)$ be $\rho = (0.20, 0.30, 0.50)$. Greater weight is assigned to high-membership conditions, while the widest outer support remains represented. With $J_{\infty,0}$ and $J_{2,0}$ denoting the uncontrolled nominal peak and RMS values on the optimization grid, the normalized components are:

$$\widehat{J}_\infty = \frac{1}{J_{\infty,0}} \sum_{a=1}^{3} \rho_a \overline{J}_{\infty,\alpha_a}^U \tag{35}$$

$$\widehat{J}_2 = \frac{1}{J_{2,0}} \sum_{a=1}^{3} \rho_a \overline{J}_{2,\alpha_a}^U \tag{36}$$

$$\widehat{W}_\infty = \frac{1}{J_{\infty,0}} \sum_{a=1}^{3} \rho_a W_{\infty,\alpha_a} \tag{37}$$

The proposed scalarized minimax objective is:

$$\mathcal{J}_{\mathrm{IT2}}(\mathrm{d}) = 0.66\widehat{J}_{\infty} + 0.24\widehat{J}_{2} + 0.10\widehat{W}_{\infty} + P_S(\mathrm{d}) + P_m(\mathrm{d}) \tag{38}$$

where the stroke penalty is:

$$P_S = 250\left[\max\left(0, \frac{\max_a \overline{J}^{U}_{S,\alpha_a}}{S_{\max}} - 1\right)\right]^2 \tag{39}$$

and a small allocation regularizer is:

$$P_m = 0.005\frac{\mathrm{sd}\left(m_{t1}, m_{t2}, m_{t3}\right)}{\mathrm{mean}\left(m_{t1}, m_{t2}, m_{t3}\right)} \tag{40}$$

The regularizer prevents numerically indistinguishable solutions from placing nearly all auxiliary mass in one device; its coefficient is two orders of magnitude smaller than the dynamic terms and does not impose equal allocation.

The scalarized objective provides one reproducible constrained design because all components are normalized by uncontrolled reference values. Increasing the peak weight would emphasize suppression of the worst resonance; increasing the RMS weight would favor broadband energy reduction; increasing the footprint-width weight would penalize sensitivity to membership uncertainty; and increasing the stroke penalty would improve feasibility margin at the cost of acceleration performance. The reported weights prioritize peak response while retaining broadband, ambiguity, and hard-travel effects, and the local Pareto diagnostic in Section 3.7 confirms that the selected solution lies in a credible peak–RMS compromise region. The minimax form is appropriate for resonant peaks and a hard stroke limit because it guarantees performance over the evaluated bounded support without assigning scenario probabilities. Its limitations are potential conservatism, sensitivity to the chosen support and finite vertex set, omission of scenario likelihood, and greater computational cost than mean- or expected-value optimization.

Four comparison cases are defined. The uncontrolled case contains no absorbers. The equal-modal case divides 23.88 kg equally, uses $r_j = 1$, and sets $\zeta_{tj} = 0.10$. The deterministic design minimizes Equation (38) using only $\theta = 1$ and no footprint-width term. The type-1 robust design replaces every inner/outer pair with the midpoint triangular cut,

$$\Theta^{T1}_{\alpha} = \frac{1}{2}\left(\Theta^{L}_{\alpha} + \Theta^{U}_{\alpha}\right) \tag{41}$$

which preserves a single membership function but discards the interval type-2 footprint.

2.6. Optimization, verification, and independent stress testing

Differential evolution uses a population of $7n_d = 63$ vectors, where $n_d = 9$. For target vector $\mathrm{d}^{(g)}_i$, the donor vector is:

$$\mathrm{v}^{(g)}_i = \mathrm{d}^{(g)}_{r_1} + F\left(\mathrm{d}^{(g)}_{r_2} - \mathrm{d}^{(g)}_{r_3}\right) \tag{42}$$

with mutually distinct indices and mutation factor $F \in [0.55, 1.0]$. Binomial crossover with probability $C_R = 0.82$ produces a trial vector. Greedy selection is:

$$\mathrm{d}_i^{(g+1)} = \begin{cases} \mathrm{u}_i^{(g)}, & \mathcal{J}\left(\mathrm{u}_i^{(g)}\right) \leq \mathcal{J}\left(\mathrm{d}_i^{(g)}\right), \\ \mathrm{d}_i^{(g)}, & \text{otherwise.} \end{cases} \tag{43}$$

Each search uses 24 generations followed by bounded local polishing. Random seeds 1102, 2203, and 3304 are assigned to the deterministic, type-1, and interval type-2 searches. The optimization frequency grid contains 125 uniformly spaced points; final frequency-response plots use 801 points.

Differential evolution was selected because the maxima over frequencies, coordinates, and uncertainty vertices, together with the activated stroke penalty, make the objective nonconvex and nonsmooth; reliable analytical gradients are therefore unavailable. Its bounded real-valued encoding and difference-based mutation are well suited to the nine continuous design variables and require fewer representation choices than a genetic algorithm. Particle swarm optimization and genetic algorithms remain valid alternatives, but no universal superiority is claimed; bounded local polishing was added to refine the best differential-evolution candidate.

Solver verification precedes the coupled-system study. For an undamped force-excited primary oscillator with mass ratio μ, the classical equal-peak formulas are:

$$r_{\text{ep}} = \frac{1}{1+\mu}, \qquad \zeta_{\text{ep}} = \sqrt{\frac{3\mu}{8(1+\mu)}} \tag{44}$$

A dense two-parameter minimax search is compared with Equation (44) for five mass ratios. This verification tests dynamic-stiffness assembly, complex solution, peak extraction, and optimization independently of the proposed fuzzy formulation.

Robust validation uses a scrambled Sobol sequence of 2,048 points over the full outer support:

$$\mathcal{U} = [0.94, 1.06] \times [0.88, 1.12] \times [0.70, 1.30] \tag{45}$$

These points are not used by any optimizer. Every design is reevaluated on 241 frequencies for each scenario. Reported statistics are the mean, 95th percentile, and maximum of scenario peak acceleration; mean and 95th percentile of scenario RMS acceleration; maximum stroke; and percentage of scenarios with $J_S > 16$ mm. A 1% central perturbation diagnostic is also calculated:

$$S_z = \frac{J_\infty(1.01z) - J_\infty(0.99z)}{0.02 J_\infty(z)} \tag{46}$$

Finally, 640 Latin-hypercube candidates in a local neighborhood of the selected interval type-2 design are screened against the stroke constraint. A candidate a dominates b when:

$$\widehat{J}_\infty^{(a)} \leq \widehat{J}_\infty^{(b)}, \quad \widehat{J}_2^{(a)} \leq \widehat{J}_2^{(b)} \tag{47}$$

with at least one strict inequality. This diagnostic shows whether the scalarized solution lies near the feasible peak–RMS trade-off rather than being an isolated numerical artifact.

3. Results

3.1. Verification against the equal-peak solution

Table 3 compares the closed-form quantities in Equation (44) with a direct numerical minimax search. The tuning ratio is recovered to the reported numerical precision for all five mass ratios. The largest damping-ratio error is 0.20%, occurring because the 101-point damping grid advances in increments of 0.2% of the central analytical value. The error is therefore exactly one grid increment and does not indicate a dynamic-stiffness discrepancy. This test is important because the same complex algebra, frequency sweep, and maximum-response operation are used in the nine-coordinate calculations.

Table 3. Verification of the frequency-response solver against classical equal-peak formulas.

Mass ratio, μ	Analytical r_{ep}	Numerical r_{ep}	Error (%)	Analytical ζ_{ep}	Numerical ζ_{ep}	Error (%)
0.01	0.990099	0.990099	0.000	0.060933	0.060933	0.000
0.03	0.970874	0.970874	0.000	0.104510	0.104510	0.000
0.05	0.952381	0.952381	<0.001	0.133631	0.133898	0.200
0.08	0.925926	0.925926	0.000	0.166667	0.167000	0.200
0.10	0.909091	0.909091	<0.001	0.184637	0.185007	0.200

Modal calculation is also a dimensional check with an internal representation. Then substituting the first natural frequency into the Rayleigh expression gives:

$$\zeta_1 = \frac{a_R}{2\omega_1} + \frac{b_R\omega_1}{2} = \frac{0.60251}{2(32.369)} + \frac{\left(3.5177 \times 10^{-4}\right)(32.369)}{2} = 0.01500 \qquad (48)$$

For the third mode, $\omega_3 = 128.847\ \mathrm{rad\,s^{-1}}$ gives $\zeta_3 = 0.02500$. The values from **Table 1** are obtained for the remaining modal damping ratios in a similar way, but they steadily rise with frequency; none is specified independently.

3.2. Optimized absorber parameters

The three optimizations converged to distinctly different allocations, as shown in **Table 4**. The objective values were 0.24397, 0.28358, and 0.29380 for the deterministic, type-1, and interval type-2 formulations, respectively. These values are meaningful only within their own scenario definitions because the deterministic objective contains one model, whereas the two robust objectives aggregate multiple cuts. The physical parameters and independent responses, rather than the raw objective values, provide the proper comparison.

Table 4. Physical parameters of the equal-modal and optimized three-absorber designs.

Design	Absorber	Mass (kg)	Tuning ratio	Damping ratio	Stiffness (kN m^{-1})	Damping (N s m^{-1})
	1	7.960	1.0000	0.1000	8.340	51.532
Equal-modal	2	7.960	1.0000	0.1000	53.611	130.651
	3	7.960	1.0000	0.1000	132.148	205.124
	1	10.411	0.9628	0.2400	10.111	155.734
Deterministic	2	10.104	0.9578	0.1588	62.426	252.259
	3	3.365	1.0295	0.0860	59.216	76.747

Table 4. *Cont.*

Design	Absorber	Mass (kg)	Tuning ratio	Damping ratio	Stiffness (kN m^{-1})	Damping (N s m^{-1})
	1	12.948	0.9005	0.2400	11.000	181.149
Type-1 robust	2	7.112	0.9715	0.1424	45.208	161.477
	3	3.820	1.0114	0.0606	64.876	60.387
	1	13.490	0.8406	0.2400	9.987	176.187
Proposed IT2 robust	2	7.393	0.9705	0.1437	46.897	169.200
	3	2.997	1.0271	0.0743	52.490	58.913

The interval type-2 design assigns 56.49%, 30.96%, and 12.55% of the auxiliary mass to absorbers 1–3:

$$\frac{\mathrm{m}_t}{23.88} \times 100 = \frac{(13.4899,\ 7.3930,\ 2.9971)}{23.88} \times 100 = (56.49,\ 30.96,\ 12.55)\% \quad (49)$$

This result departs substantially from the equal 33.33% allocation. It also detunes the first absorber downward to $r_1 = 0.8406$, the active lower bound is approached but not reached, while the second and third ratios remain close to their target modes. The first device is consequently used as a broad low-frequency support rather than as a narrow resonance splitter. To demonstrate the conversion from nondimensional to physical variables, the first interval type-2 absorber has:

$$k_{t1} = 13.4899\,[0.840606(2\pi)(5.151715)]^2 = 9.9875 \times 10^3\ \mathrm{N\,m^{-1}} \quad (50)$$

$$c_{t1} = 2(0.24)(13.4899)(0.840606)(2\pi)(5.151715) = 176.187\ \mathrm{N\,s\,m^{-1}} \quad (51)$$

Both calculations reproduce **Table 4** after rounding. The damping ratio of absorber 1 reaches the specified upper bound in all three optimized designs. This is not an unconstrained request for excessive damping: the corresponding coefficient is only 176.2 N s m^{-1} because the first absorber is light and tuned to a low frequency. Additionally, both absorbers 2 and 3 still employ interior damping solutions demonstrating that this optimization did not simply drive every dissipation variable to its maximum limit.

The concentration of 56.49% of the auxiliary mass in absorber 1 follows from the first mode having the largest uncertainty-induced downward frequency shift and strong participation in the monitored responses. Additional first-absorber mass increases control authority and bandwidth, while the tuning ratio of 0.8406 protects the lower-frequency edge and reduces sensitivity to resonance migration. Absorbers 2 and 3 remain close to their target modes to preserve upper-band control. This unequal allocation and selective detuning therefore arise from the combined peak, RMS, footprint-width, and stroke objectives rather than from a classical equal-peak condition.

3.3. Nominal frequency response

Figure 3 shows the fine-grid nominal responses at coordinates 2, 4, and 6. The uncontrolled system exhibits sharp resonance amplification near its first three modes. Each absorber bank lowers the dominant peaks, although the response shapes differ. Q-modulus tuning produces deep notches with broad adjacent lobes. The deterministic design gives the lowest nominal maximum, whereas both robust designs accept a moderate increase in nominal acceleration to improve response flatness under detuning.

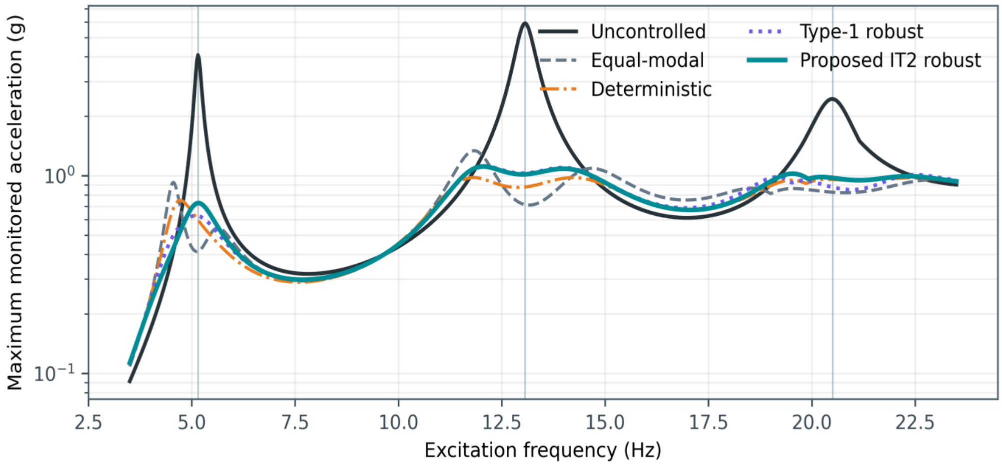

Figure 3. Nominal acceleration frequency-response functions at the three monitored coordinates for the uncontrolled and controlled systems.

The fine-grid nominal metrics in **Table 5** were evaluated on 801 frequencies and are separate from the 125-point optimization grid. The interval type-2 design reduces the nominal peak from 5.898 g to 1.114 g, an 81.11% reduction. Its RMS value is 0.628 g, 43.61% below the uncontrolled level, and its maximum nominal stroke is 14.119 mm. The deterministic design improves the nominal peak by a further 12.01% relative to the proposed design but uses 16.264 mm of travel at the nominal parameter point. That travel already exceeds the design limit before primary-system uncertainty is introduced.

Table 5. Fine-grid nominal response over 3.5–23.5 Hz.

Design	Peak acceleration (g)	RMS acceleration (g)	Maximum stroke (mm)	Peak reduction from uncontrolled (%)
Uncontrolled	5.898	1.114	—	—
Equal-modal	1.340	0.601	31.208	77.29
Deterministic	0.980	0.605	16.264	83.38
Type-1 robust	1.120	0.619	13.516	81.00
Proposed IT2 robust	1.114	0.628	14.119	81.11

For a response-ratio interpretation, the nominal peak attenuation of the proposed design is:

$$L_A = 20\log_{10}\left(\frac{1.11396}{5.89768}\right) = -14.48\ \text{dB} \tag{52}$$

The decibel expression is not an acoustic sound-pressure level; it is a compact logarithmic ratio of acceleration amplitudes. The arithmetic reduction and the logarithmic reduction describe the same calculated response.

3.4. Nested fuzzy response envelopes

Figure 4 compares the frequency-response envelopes produced by the full outer support. The uncontrolled envelope is broad near the first resonance because the approximate modal frequency scales as:

$$f_r\left(\theta_m, \theta_k\right) \approx f_{r0}\sqrt{\frac{\theta_k}{\theta_m}} \tag{53}$$

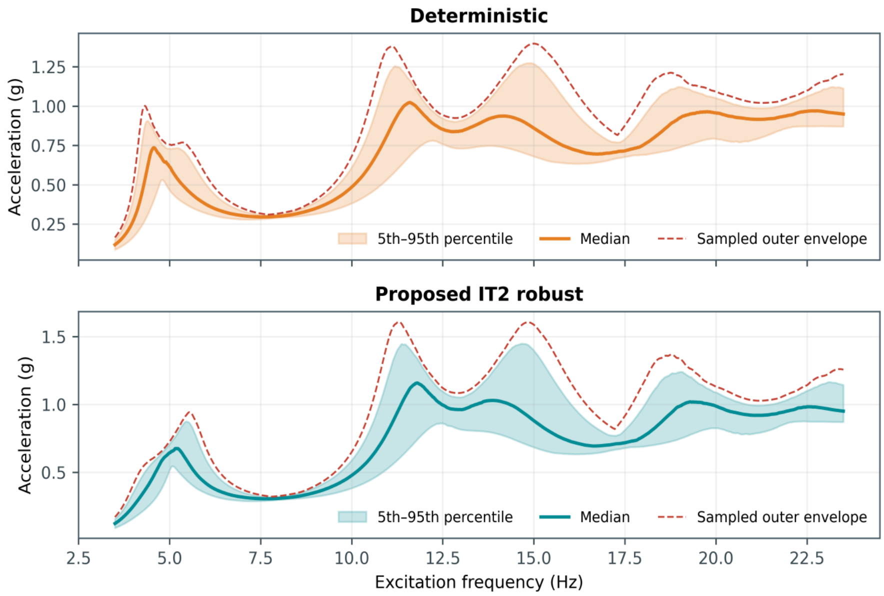

Figure 4. Outer-support acceleration envelopes for the uncontrolled, deterministic, type-1 robust, and proposed interval type-2 designs.

At the most adverse outer combination $\theta_k = 0.88$ and $\theta_m = 1.06$, the frequency scale becomes $\sqrt{0.88/1.06} = 0.9111$. Thus, the first nominal mode can shift from 5.1517 Hz to approximately 4.6936 Hz even before damping variation is considered. The proposed first-absorber ratio of 0.8406 is consistent with protecting the lower side of this enlarged interval while absorbers 2 and 3 control the middle and upper modal regions.

At $\alpha = 0$, the proposed design gives an inner-vertex peak of 1.403 g and an outer-vertex peak of 1.709 g, so the footprint contribution is 0.306 g. At $\alpha = 0.5$, the corresponding values are 1.240 g and 1.365 g, giving 0.125 g. The footprint width collapses to zero at $\alpha = 1$, where both sets reduce to the nominal point and the peak is 1.114 g. These nested values behave as expected:

$$\begin{aligned} W_{\infty,0} &= 1.70894 - 1.40282 = 0.30612 \text{ g}, \\ W_{\infty,0.5} &= 1.36518 - 1.24001 = 0.12517 \text{ g} \end{aligned} \tag{54}$$

The outer-vertex RMS values at $\alpha = 0$, 0.5, and 1 are 0.6935, 0.6577, and 0.6277 g, respectively. The maximum outer-vertex travel on the 125-point optimization grid is 16.005 mm. This is 0.005 mm, or 0.03%, above the nominal engineering limit because the quadratic penalty permits a small numerical tolerance. On the denser independent 241-point stress-test scenarios, the maximum is 15.992 mm, as reported below. A design should therefore be interpreted with the stated numerical resolution rather than with more precision than the frequency grid supports.

3.5. Independent outer-support stress test

Table 6 contains the principal out-of-sample comparison. These 2,048 Sobol scenarios fill the three-dimensional outer support without reusing optimizer vertices. The uncontrolled system has a mean scenario peak of 6.058 g and a maximum of 9.005 g. Equal-modal tuning lowers those values substantially, but every scenario exceeds the 16 mm stroke limit and the maximum travel reaches 42.614 mm. This result demonstrates why attenuation alone is an incomplete design criterion.

Table 6. Independent 2,048-scenario outer-support stress-test results.

Design	Mean peak (g)	95th peak (g)	Maximum peak (g)	Mean RMS (g)	95th RMS (g)	Maximum stroke (mm)	Stroke exceedance (%)
Uncontrolled	6.058	8.045	9.005	1.126	1.324	—	—
Equal-modal	1.452	1.836	2.247	0.606	0.642	42.614	100.00
Deterministic	1.112	1.291	1.437	0.608	0.642	21.458	55.42
Type-1 robust	1.273	1.496	1.689	0.623	0.660	17.195	2.05
Proposed IT2 robust	1.262	1.484	1.682	0.632	0.671	15.992	0.00

Relative to the uncontrolled case, the proposed interval type-2 design reduces the mean, 95th-percentile, and maximum scenario peaks by 79.16%, 81.56%, and 81.33%, respectively. The maximum-peak calculation is:

$$R_{\max} = 100\left(1 - \frac{1.68159}{9.00455}\right) = 81.33\% \tag{55}$$

Mean RMS acceleration decreases by 43.87%. Relative to the deterministic optimum, the proposed design has a 13.53% higher mean peak and a 17.04% higher maximum peak, but it changes the stroke-exceedance probability observed in the finite scenario set from 55.42% to zero. The type-1 robust solution is closer: the interval type-2 design lowers its mean peak by 0.82%, its maximum peak by 0.43%, and its maximum stroke by 6.99%, while increasing mean RMS by 1.49%. The important change is that the 1.203 mm reduction in maximum travel moves the complete evaluated set to the feasible side of the limit.

Figure 5 shows that the deterministic response distribution is shifted toward lower acceleration, but its travel distribution crosses the limit over a large fraction of the support. The type-1 distribution nearly satisfies the limit, although a small upper tail remains. The interval type-2 distribution terminates immediately below 16 mm. Since the coordinates of a stress-test location are low-discrepancy samples of a bounded epistemic set, exceedance percentages quantified relative to this location correspond to empirical coverage probabilities; we do not claim that they represent physical failure probabilities.

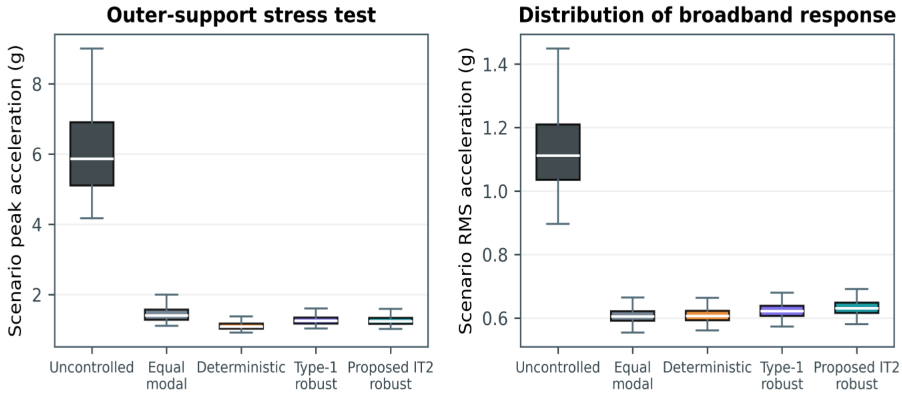

Figure 5. Distributions of scenario peak acceleration and maximum relative stroke in the independent outer-support stress test.

3.6. Critical stroke response

The critical uncontrolled scenario is $\theta = (1.05767, 0.88272, 0.72451)$. The combination of high mass, low stiffness, and low damping shifts the first resonance below 4.30 Hz, where absorber 1 governs the controlled response (**Figure 6**).

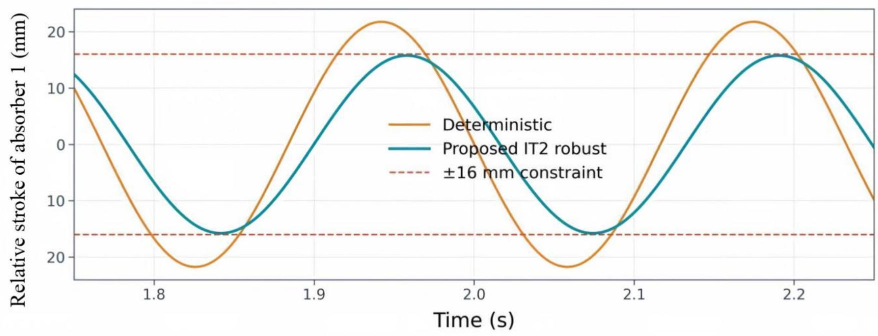

Figure 6. Relative-stroke histories of absorber 1 at 4.30 Hz for the critical outer-support scenario; verified peak amplitudes used for the margin calculations are reported in **Table 6**.

Using the independently verified **Table 6** maximum amplitudes, the stroke margins are −5.458 mm for the deterministic design and +0.008 mm for the interval type-2 design:

$$\Delta S_{\text{det}} = 16.00 - 21.458 = -5.458 \text{ mm},$$
$$\Delta S_{\text{IT2}} = 16.00 - 15.992 = +0.008 \text{ mm} \tag{56}$$

These verified steady-state amplitudes correspond to peak-to-peak travels of 42.916 and 31.984 mm for the deterministic and interval type-2 designs, respectively, assuming symmetric motion.

3.7. Local sensitivity and Pareto diagnostic

Finally, normalized measures from Equation (46) of central perturbation are reported in **Table 7** and **Figure 7**. Nominal worst response signs indicate the local direction; magnitudes are ratios that quantify how much the maximum response increases because of a relative increase in one variable. These finite-difference diagnostics, instead of derivatives of a globally smooth function is because the identity of either the active frequency or coordinate monitored can dynamically change.

Table 7. Normalized 1% central sensitivities of the proposed design.

Variable	Sensitivity	Variable	Sensitivity
Primary mass multiplier	0.810	TMD mass 1	0.155
Primary stiffness multiplier	−1.162	TMD mass 2	−0.199
Primary damping multiplier	−0.193	TMD mass 3	0.044
Tuning ratio 1	−0.143	TMD damping 1	−0.051
Tuning ratio 2	1.355	TMD damping 2	0.233
Tuning ratio 3	0.013	TMD damping 3	−0.001

The largest magnitude is associated with tuning ratio 2 ($S = 1.355$), followed by the primary stiffness multiplier ($S = -1.162$) and primary mass multiplier ($S = 0.810$). A 1% upward perturbation of r_2 therefore tends locally to increase the active peak, whereas a 1% upward stiffness perturbation tends to decrease it. The near-zero values for r_3 and

ζ_{t3} show that the nominal active peak is not governed by the third absorber. This does not make absorber 3 unnecessary: it contributes to the third modal region and to the outer-support maximum, which need not share the nominal active point.

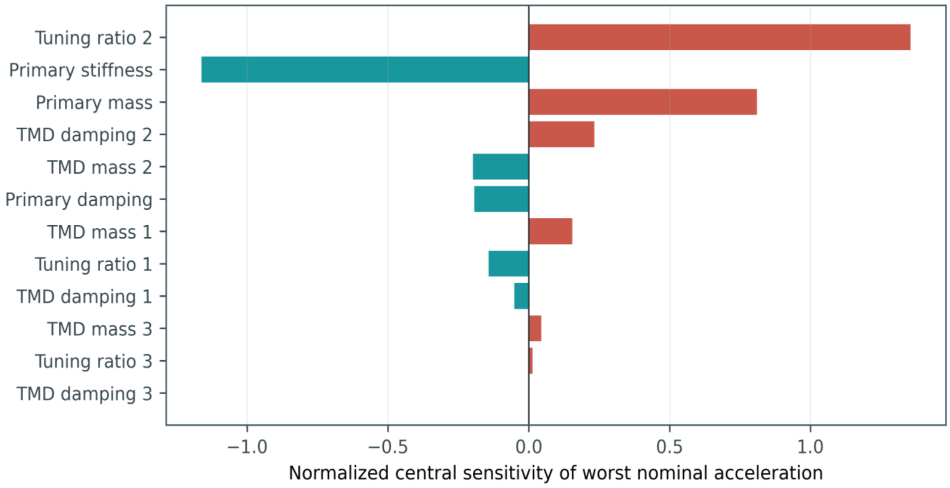

Figure 7. Normalized central sensitivities of the proposed interval type-2 design.

The local design cloud contained 359 candidates satisfying the stroke criterion, of which five were nondominated in normalized peak–RMS space. **Figure 8** shows the feasible and infeasible candidates together with the selected design. Its normalized coordinates are $(0.29356, 0.62472)$. The point lies adjacent to the short nondominated front, supporting the scalarization as a reasonable peak-oriented compromise rather than an isolated search result.

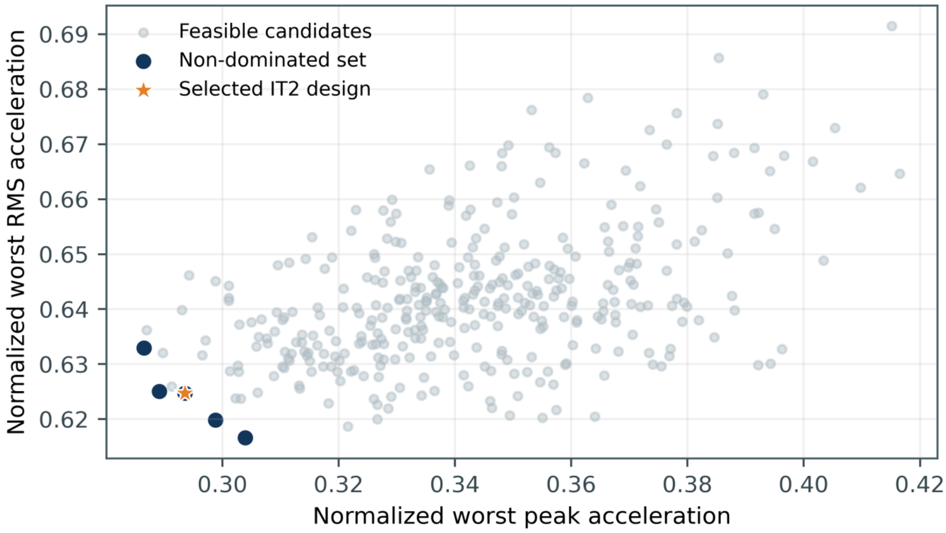

Figure 8. Local peak–RMS trade-off around the proposed design; the nondominated subset is identified after applying the stroke constraint.

4. Discussion

4.1. Interpretation of the robust design mechanism

The results support three connected interpretations. First, uncertainty changes the useful role of the first absorber. Under nominal optimization, absorber 1 receives 10.411 kg and is tuned at 96.28% of the first modal frequency. The interval type-2 solution increases its mass to 13.490 kg and lowers the ratio to 84.06%. The mass increase raises the device authority, while downward detuning protects the low-frequency edge produced by high primary mass and low stiffness. Relative to the deterministic design, the change in the first tuning ratio is:

$$\Delta r_1 = 100\left(\frac{0.840606}{0.962805} - 1\right) = -12.69\% \tag{57}$$

The second ratio changes by only +1.33%, and the third changes by −0.23%. Robustification is therefore not equivalent to applying one common detuning factor to the entire bank. It acts mode by mode according to the combination of uncertainty, force participation, monitored coordinates, and travel demand.

Second, the results distinguish low nominal response from implementable robust response. The deterministic optimum gives the smallest acceleration statistics because it is specialized to one parameter point. However, the same narrow tuning demands excessive absorber travel when the primary resonance shifts. The equal-modal design is more extreme: it produces the smallest mean RMS among the controlled cases but exceeds the travel limit in all 2,048 scenarios. A design selected only from an RMS or nominal-peak column would therefore be misleading. The quadratic stroke penalty in Equation (39) changes the optimization landscape only after the limit is exceeded, thereby excluding dynamically attractive but infeasible antiresonant solutions.

Third, the interval type-2 footprint defines an actionable robustness boundary. The midpoint type-1 design still exceeds the 16 mm stroke limit in 42 of 2,048 scenarios (2.05%) and therefore performs worse in feasibility than the interval type-2 design. Preserving both inner and outer membership functions changes the mass distribution and first tuning sufficiently to eliminate those exceedances over the evaluated support. The acceleration cost relative to the type-1 design is modest: the mean and maximum peaks improve slightly, while the mean RMS increases by 0.0093 g. Thus, the footprint-width term does not improve every response uniformly; it steers the search away from configurations whose feasibility depends strongly on one selected membership width.

4.2. Relation to existing robust absorber design

Set-based optimization produced a less specialized design than the nominal optimum, consistent with robust absorber studies [15,37,38]. The formulation requires nominal multipliers and two plausible half-widths rather than defensible probability distributions; these bounds can be obtained from tolerances, sparse observations, or structured expert judgment.

This interval type-2 formulation extends type-1 fuzzy criteria by retaining a range of membership grades [16, 18]. Equations (32)–(37) propagate the performance gap between the narrow and wide interpretations. At $\alpha = 1$, the inner and outer vertices coincide; at each nondegenerate α-plane, eight inner and eight outer vertices are evaluated.

The technique can be used with classical tuning [6–9], as well as MTMD/TMDI developments [39]. Verification and bounds are supported through equal-peak formulas, and the coupled model supports arbitrary forces, outputs, unequal masses, and travel. Alternative absorbers require only modified augmented matrices, not revised α-plane aggregation.

4.3. Numerical reliability and reproducibility

Several choices were made to reduce the chance that the reported solution is a frequency-grid or optimizer artifact. The basic solver was checked against an analytical minimax result. Optimization used fixed bounds and reported seeds. Fine nominal curves used 801 frequencies, while the independent test used 241 frequencies for each of 2,048 scenarios. The latter entails:

$$N_{solve} = 4(2,048)(241) = 1,974,272 \tag{58}$$

controlled complex linear solves for the four absorber designs, in addition to the uncontrolled evaluation. Each controlled solve involves a 9×9 complex matrix. The local 640-candidate diagnostic then checked whether the selected solution occupied a credible region of the feasible peak–RMS trade-off. Together, these tests are stronger than reporting a single optimization trace.

Nevertheless, vertex propagation is exact for the uncertainty boxes only if the response extrema occur at vertices. Dynamic response is not generally monotonic in mass, stiffness, and damping, so the optimizer's vertex set is a tractable minimax approximation. The independent interior Sobol assessment is therefore essential. In the present calculation, it found no travel value above the largest outer-vertex level after accounting for grid resolution. For a safety-critical installation, adaptive interval subdivision or verified global optimization should replace the finite vertex and sampling checks.

All dimensional inputs, membership widths, α-levels, weights, bounds, objective coefficients, frequency grids, and resulting physical absorber parameters are reported in the article. The computational model and numerical results are provided in tables and figures and do not rely on external experimental data. This presentation supports independent reproduction and audit of the numerical study.

4.4. Practical implications and limitations

Stroke feasibility is more restrictive than the nominal plausibility of the absorber parameters. The verified interval type-2 maximum of 15.992 mm leaves only a 0.008 mm margin below the 16 mm limit. This margin is insufficient for direct manufacture without additional allowance for tolerances, unmodeled nonlinearities, and installation variability.

The results presented are for a linear time-invariant, coherently forced model neglecting other nonlinear as well as temperature, transient, and speed-dependent effects. Shared property multipliers and static attachments also eliminate uncertainties particular to components and placement; extensions for these will be required by applications and installation rules.

Recent ensemble-optimization studies likewise emphasize that robust TMD performance depends on how uncertainty scenarios are aggregated [40]. Here, the α-plane minimax aggregation is selected to enforce the bounded-support interpretation.

Validation should identify a six-coordinate frame and test an adjustable absorber bank under swept-sine excitation. Measured peak/RMS acceleration and travel should be compared with α-plane envelopes before application-specific claims.

5. Conclusion

An interval type-2 fuzzy α-plane minimax method was developed for the constrained co-design of three passive tuned mass dampers on a six-degree-of-freedom coupled system. The model integrates nonuniform mass allocation, modal tuning, absorber damping, broadband acceleration, membership-function ambiguity, and a 16 mm relative-stroke requirement in one optimization problem.

The proposed design allocates 13.490, 7.393, and 2.997 kg to the three devices and adopts tuning ratios 0.8406, 0.9705, and 1.0271. In 2,048 independent outer-support scenarios, it reduces mean peak acceleration by 79.16% and maximum peak acceleration by 81.33% relative to the uncontrolled system. Its maximum evaluated stroke is 15.992 mm and no scenario exceeds the limit. By comparison, the deterministic optimum exceeds the stroke limit in 55.42% of scenarios and the midpoint type-1 robust design exceeds it in 2.05%.

The main conclusion is that uncertainty in the membership function itself can alter a passive absorber design enough to determine feasibility. The benefit does not arise from uniformly conservative tuning: it arises from reallocating mass and selectively detuning the first absorber while preserving near-modal tuning for the other two. This method is appropriate when there are bounded engineering data available and the use of probability distributions cannot be justified. Experimental identification for actual systems, explicit manufacturing margins, nonlinear travel stops and component-wise uncertainty still necessitate thorough attention prior to application to functional machinery.

Author contributions: Conceptualization, SIM and YN; methodology, YN; software, YN and PW; validation, YN, SIM, SAB and PW; formal analysis, YN; investigation, YN and SIM; resources, SAB and AV; data curation, YN and PW; writing—original draft preparation, YN and SIM; writing—review and editing, YN, SAB, PW and AV; visualization, YN and PW; supervision, AV; project administration, YN. All authors have read and agreed to the published version of the manuscript.

Funding: This study received no external funding.

Institutional review board statement: Not applicable.

Informed consent statement: Not applicable.

Data availability statement: All data needed to reproduce the computational study are contained within the article itself, including model inputs, numerical settings corresponding to different design variables, and equations from tabulated results and all graphical results. No supplementary dataset is required.

Conflict of interest: The authors declare no conflict of interest.

AI use statement: During revision, the authors used ChatGPT (OpenAI) to assist with language editing and verification. The tool was not used to generate or modify the study data, computational results, visualization, or scientific conclusions. The authors reviewed and edited all the content and take full responsibility for the content of the publication.

References

1. Yang F, Sedaghati R, Esmailzadeh E. Vibration suppression of structures using tuned mass damper technology: A state-of-the-art review. Journal of Vibration and Control. 2022; 28(7–8): 812–836. doi: 10.1177/1077546320984305
2. Naderpour H, SoltaniMatin A, Kheyroddin A, et al. Optimizing seismic performance of tuned mass dampers at various levels in reinforced concrete buildings. Buildings. 2024; 14(8): 2443. doi: 10.3390/buildings14082443
3. Chan PT. Optimizing distribution of multiple tuned mass dampers for building structures with inverse element exchange method. Earthquake Engineering and Engineering Vibration. 2025; 24: 187–199. doi: 10.1007/s11803-025-2301-0
4. Cao HQ. A comparative study on the effectiveness, robustness and mistuning sensitivity of upgraded tuned mass dampers in mitigating the dynamic response of civil structures. Archive of Applied Mechanics. 2025; 95: 71. doi: 10.1007/s00419-025-02781-z
5. Richiedei D, Tamellin I, Trevisani A. Beyond the tuned mass damper: A comparative study of passive approaches to vibration absorption through antiresonance assignment. Archives of Computational Methods in Engineering. 2022; 29: 519–544. doi: 10.1007/s11831-021-09583-w
6. Warburton GB. Optimum absorber parameters for various combinations of response and excitation parameters. Earthquake Engineering & Structural Dynamics. 1982; 10(3): 381–401. doi: 10.1002/eqe.4290100304
7. Krenk S. Frequency analysis of the tuned mass damper. Journal of Applied Mechanics. 2005; 72(6): 936–942. doi: 10.1115/1.2062867
8. Nishihara O, Asami T. Closed-form solutions to the exact optimizations of dynamic vibration absorbers (minimizations of the maximum amplitude magnification factors). Journal of Vibration and Acoustics. 2002; 124(4): 576–582. doi: 10.1115/1.1500335
9. Asami T, Nishihara O, Baz AM. Analytical solutions to H_∞ and H_2 optimization of dynamic vibration absorbers attached to damped linear systems. Journal of Vibration and Acoustics. 2002; 124(2): 284–295. doi: 10.1115/1.1456458
10. Zuo L, Nayfeh SA. Minimax optimization of multi-degree-of-freedom tuned-mass dampers. Journal of Sound and Vibration. 2004; 272(3–5): 893–908. doi: 10.1016/S0022-460X(03)00500-5
11. Zuo L, Nayfeh SA. Optimization of the individual stiffness and damping parameters in multiple-tuned-mass-damper systems. Journal of Vibration and Acoustics. 2005; 127(1): 77–83. doi: 10.1115/1.1855929
12. Abé M, Fujino Y. Dynamic characterization of multiple tuned mass dampers and some design formulas. Earthquake Engineering & Structural Dynamics. 1994; 23(8): 813–835. doi: 10.1002/eqe.4290230802
13. Hoang N, Warnitchai P. Design of multiple tuned mass dampers by using a numerical optimizer. Earthquake Engineering & Structural Dynamics. 2005; 34(2): 125–144. doi: 10.1002/eqe.413
14. Ok SY, Song J, Park KS. Development of optimal design formula for bi-tuned mass dampers using multi-objective optimization. Journal of Sound and Vibration. 2009; 322(1–2): 60–77. doi: 10.1016/j.jsv.2008.11.023
15. Marano GC, Sgobba S, Greco R, et al. Robust optimum design of tuned mass dampers devices in random vibrations mitigation. Journal of Sound and Vibration. 2008; 313(3–5): 472–492. doi: 10.1016/j.jsv.2007.12.020
16. Marano GC, Quaranta G. Robust optimum criteria for tuned mass dampers in fuzzy environments. Applied Soft Computing. 2009; 9(4): 1232–1243. doi: 10.1016/j.asoc.2009.03.010
17. Song C, Xiao R, Jiang Z, et al. Active-learning Kriging-assisted robust design optimization of tuned mass dampers: Vibration mitigation of a steel-arch footbridge. Engineering Structures. 2024; 303: 117502. doi: 10.1016/j.engstruct.2024.117502
18. Marano GC, Quaranta G, Sgobba S. Fuzzy-entropy based robust optimization criteria for tuned mass dampers.

Earthquake Engineering and Engineering Vibration. 2010; 9: 285–294. doi: 10.1007/s11803-010-0013-5
19. Yu H, Gillot F, Ichchou MN. Reliability based robust design optimization for tuned mass damper in passive vibration control of deterministic/uncertain structures. Journal of Sound and Vibration. 2013; 332(9): 2222–2238. doi: 10.1016/j.jsv.2012.12.014
20. Most T, Zabel V, Das RR, et al. An efficient uncertainty quantification approach for robust design of tuned mass dampers in linear structural dynamics. Applied Sciences. 2025; 15(17): 9329. doi: 10.3390/app15179329
21. Pellizzari F, Marano GC, Palmeri A, et al. Robust optimization of MTMD systems for the control of vibrations. Probabilistic Engineering Mechanics. 2022; 70: 103347. doi: 10.1016/j.probengmech.2022.103347
22. Ontiveros-Pérez SP, Miguel LFF. Reliability-based optimum design of multiple tuned mass dampers for minimization of the probability of failure of buildings under earthquakes. Structures. 2022; 42: 144–159. doi: 10.1016/j.istruc.2022.06.015
23. Cetin H, Aydin E, Ozturk B. Multiple tuned mass damper design for the mitigation of cantilever beam response. ASCE-ASME Journal of Risk and Uncertainty in Engineering Systems, Part A: Civil Engineering. 2025; 11(3): 04025052. doi: 10.1061/AJRUA6.RUENG-1502
24. Meng D, Hu Z, Guo J, et al. An uncertainty-based structural design and optimization method with interval Taylor expansion. Structures. 2021; 33: 4492–4500. doi: 10.1016/j.istruc.2021.07.007
25. Zakian P, Bakhshpoori T. Optimal design of multiple tuned mass dampers for controlling the earthquake response of randomly excited structures. Acta Mechanica. 2024; 235(1): 511–532. doi: 10.1007/s00707-023-03749-2
26. Mendel JM, John RIB. Type-2 fuzzy sets made simple. IEEE Transactions on Fuzzy Systems. 2002; 10(2): 117–127. doi: 10.1109/91.995115
27. Mendel JM, John RIB, Liu F. Interval type-2 fuzzy logic systems made simple. IEEE Transactions on Fuzzy Systems. 2006; 14(6): 808–821. doi: 10.1109/TFUZZ.2006.879986
28. D'Alterio P, Garibaldi JM, John RI, et al. Constrained interval type-2 fuzzy sets. IEEE Transactions on Fuzzy Systems. 2021; 29(5): 1212–1226. doi: 10.1109/TFUZZ.2020.2970911
29. Beyer HG, Sendhoff B. Robust optimization—A comprehensive survey. Computer Methods in Applied Mechanics and Engineering. 2007; 196(33–34): 3190–3218. doi: 10.1016/j.cma.2007.03.003
30. Zang C, Friswell MI, Mottershead JE. A review of robust optimal design and its application in dynamics. Computers & Structures. 2005; 83(4–5): 315–326. doi: 10.1016/j.compstruc.2004.10.007
31. Storn R, Price K. Differential evolution—A simple and efficient heuristic for global optimization over continuous spaces. Journal of Global Optimization. 1997; 11: 341–359. doi: 10.1023/A:1008202821328
32. Deb K, Pratap A, Agarwal S, et al. A fast and elitist multiobjective genetic algorithm: NSGA-II. IEEE Transactions on Evolutionary Computation. 2002; 6(2): 182–197. doi: 10.1109/4235.996017
33. Saltelli A, Annoni P, Azzini I, et al. Variance based sensitivity analysis of model output: Design and estimator for the total sensitivity index. Computer Physics Communications. 2010; 181(2): 259–270. doi: 10.1016/j.cpc.2009.09.018
34. Ozturk B, Cetin H, Aydin E. Optimum vertical location and design of multiple tuned mass dampers under seismic excitations. Structures. 2022; 41: 1141–1163. doi: 10.1016/j.istruc.2022.05.014
35. Cao HQ, Tran NA. Multi-objective optimal design of double tuned mass dampers for structural vibration control. Archive of Applied Mechanics. 2023; 93(5): 2129–2144. doi: 10.1007/s00419-023-02376-6
36. Li C, Pan H, Cao L. Pendulum-type tuned tandem mass dampers-inerters for crosswind response control of super-tall buildings. Journal of Wind Engineering and Industrial Aerodynamics. 2024; 247: 105706. doi: 10.1016/j.jweia.2024.105706
37. Brandão FdS, de Almeida AK, Miguel LFF. Optimum design of single and multiple tuned mass dampers for vibration control in buildings under seismic excitation. International Journal of Structural Stability and Dynamics. 2022; 22(8): 2250078. doi: 10.1142/S021945542250078X
38. Rossato BB, Miguel LFF. Robust optimum design of tuned mass dampers for high-rise buildings subject to wind-induced vibration. Numerical Algebra, Control and Optimization. 2023; 13(1): 154–168. doi: 10.3934/naco.2021060
39. Wang L, Zhou Y, Shi W. Random crowd-induced vibration in footbridge and adaptive control using semi-active TMD including crowd–structure interaction. Engineering Structures. 2024; 306: 117839. doi: 10.1016/j.engstruct.2024.117839
40. Chowdhury S, Adhikari S. In-sample versus ensemble optimisation of tuned mass dampers for structures with uncertainties. Probabilistic Engineering Mechanics. 2026; 85: 103982. doi: 10.1016/j.probengmech.2026.103982